# Near-Field Characterization of Graphene Plasmons by Photo-Induced Force Microscopy

*Jianxun Liu, Sung Park, Derek Nowak, Mengchuan Tian, Yanqing Wu, Hua Long, Kai Wang, Bing Wang,\* and Peixiang Lu\**

The near-field features of graphene plasmons (GPs) using a recently developed photo-induced force microscopy (PiFM) technique are characterized here. The GPs are excited by a mid-infrared laser beam obliquely incident on graphene suspended over a metallic grating with a dielectric spacer. The PiFM records the optical force yielded by the interaction between the electric field of GPs in the normal direction and dipoles in a metallic tip. The magnitude of the optical force is proportional to the field intensity of the GPs. By detecting the interference pattern of GPs on the grating trenches, the wavelength and propagation distance of GPs can be obtained. The PiFM technique demonstrated here provides a powerful tool to precisely characterize GPs in a deeply subwavelength scale and aid in the design of nanoscale optical devices based on graphene.

## 1. Introduction

Surface plasmon polaritons (SPPs) are electromagnetic waves that can be guided at the interface between metal and dielectric, which tend to be highly concentrated on the metal surface and possess remarkably strong field intensity. SPPs could find important applications in many fields ranging from nanoscale optical transport to near-field imaging and scattering enhancement.[1–3] With respect to the propagating SPPs on metals, the short propagation distance may pose a major impediment to real applications.[4,5] Recently, there have been considerable efforts dedicated to investigating SPPs on graphene, which is known as graphene plasmons (GPs).[6–10] Graphene is a 2D material

that can support SPPs subject to infrared and THz frequencies. By comparing with SPPs on metals, GPs manifest unique properties such as stronger field confinement, more flexible tunability, and relatively less propagation loss.[11–14]

Due to the large mismatch of wave vectors, GPs are hard to excite by light waves in free space. The mismatch of wave vectors could be efficiently compensated for by periodic tuning, such as coupling the graphene layer to a subwavelength grating, fabricating the graphene as arrays, and setting the graphene to wavy patterns.[15–21] Characterizing GPs is challenging due to the strong confinement on graphene. The field of GPs is concentrated on graphene within an extremely short distance, orders of magnitude less than the exciting wavelength in free space. The direct observation of GPs in experiment was first implemented recently by using a scattering-type scanning near-field optical microscopy (s-SNOM).[22–24] However, the near-field scattering signal typically contains background contributions from neighboring sample locations and regions apart from the tip apex, which requires sophisticated background suppression and image deconvolution techniques.[23,25]

Recently, a new characterization technique named photo-induced force microscopy (PiFM) was invented based on the optical force and force gradient detection.[26–28] PiFM combines an atomic force microscopy (AFM) technique with conventional optical microscope, and it can probe the interaction of light and materials at nanoscale.[29,30] By comparing with s-SNOM, PiFM detects the photo-induced force signal at the direct mode,[27] or the force gradient signal by using the sideband mode rather than light field directly.[31] Because the PiFM sideband mode enables to observe only the distance-dependent force gradient which relates to the field gradient force rather than the constant background force at nanoscale, it is insensitive to the far-field scattering contributions which is nearly constant under the tip apex. As PiFM is purely force and force gradient based, the technique does not require optical detectors to collect the scattered near-field light, making the technique easier to operate and more robust against the environmental conditions. The strong localized field of plasmons is known to be more sensitive along the vertical direction, so the field force gradient information of plasmons can be measured with a low background noise, high resolution, and broundband range wavelength response by PiFM. In this work, we focus at investigating GPs on monolayer graphene covering a metallic

Dr. J. Liu, Prof. H. Long, Prof. K. Wang, Prof. B. Wang, Prof. P. Lu
Wuhan National Laboratory for Optoelectronics and School of Physics
Huazhong University of Science and Technology
Wuhan 430074, China
E-mail: wangbing@hust.edu.cn; lupeixiang@hust.edu.cn
Dr. S. Park, Dr. D. Nowak
Molecular Vista
6840 Via Del Oro, Suite 110, San Jose, CA 95119, USA
Dr. M. Tian, Prof. Y. Wu
Wuhan National High Magnetic Field Center and School of Electrical and Electronic Engineering
Huazhong University of Science and Technology
Wuhan 430074, China
Prof. P. Lu
Laboratory of Optical Information Technology
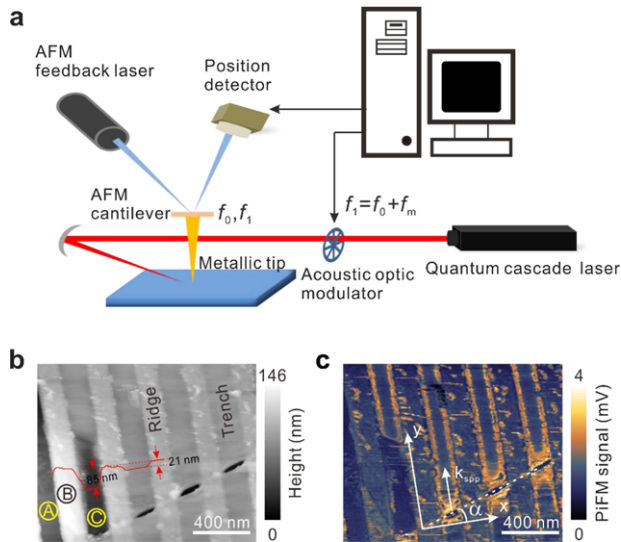Wuhan Institute of Technology
Wuhan 430205, China
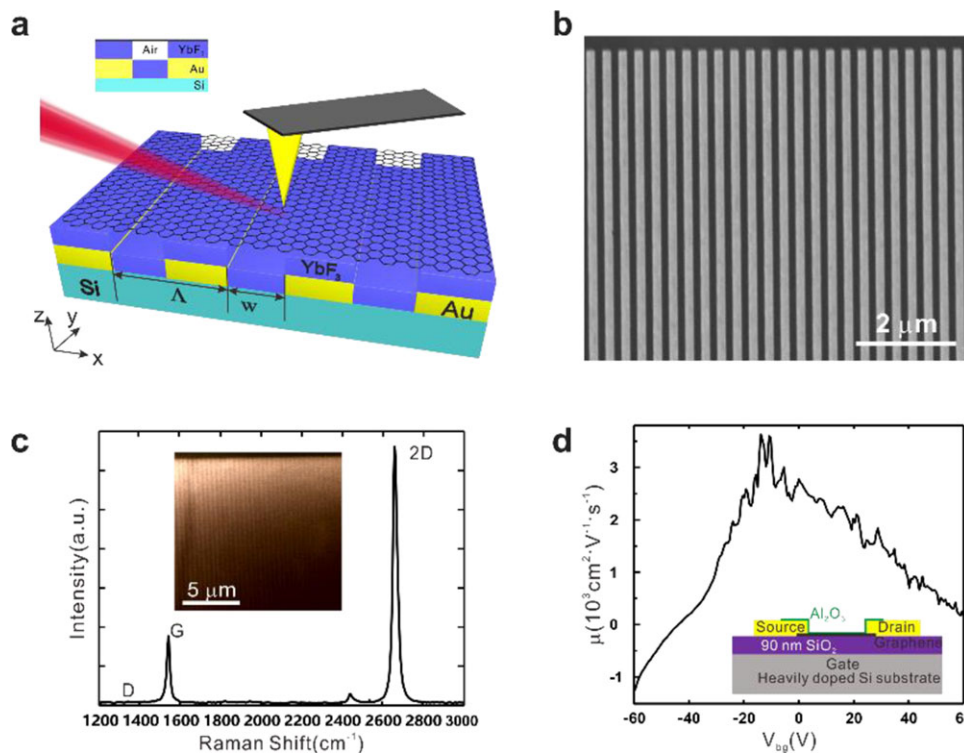
**Figure 1.** a) Schematic of the gold grating covered by YbF$_3$ layer and monolayer graphene. The inset shows the front view of the structure. YbF$_3$ thickness between the grating and graphene is 70 nm. The transverse electrical field component of the incident laser is parallel to the x-axis. b) SEM image of the gold grating. The period and the trench width of EBL fabricated grating is 330 and 180 nm, respectively. c) Raman spectrum of graphene on the top of the structure. Inset shows an optical image of the sample by a 50× objective lens. d) Electronic mobility measurement by a field effect device, which defines the field effect mobility of the graphene is close to 3000 cm$^2$ V$^{-1}$ s$^{-1}$.

grating with a dielectric spacer by using the PiFM technique. By detecting the optical force gradient between the electric field of GPs and the dipole at a metallic tip, we can characterize the general properties of GPs including the field distribution and spectral features. The study provides a new approach to characterize GPs on the nanoscale.

## 2. Result and Discussion

The geometry of the structure utilized to generate GPs is shown in **Figure 1**a. A grating of gold is fabricated on silicon substrate with a period of $\Lambda$. The width of the trenches of the grating is denoted by $w$. A metallic tip is close to the sample surface and scatters the incident light to excite the GPs. A dielectric spacer of YbF$_3$ is evaporated on the grating which has a relative permittivity $\varepsilon_d = 2.25$ around the wavelength $\lambda = 7$ $\mu$m. A scanning electron microscopy (SEM) picture of the metallic grating is shown in Figure 1b. The period of the grating is $\Lambda = 330$ nm and the width of trenches is $w = 180$ nm. The height of the gold ridges is given by $h_m = 75$ nm. The thicknesses of YbF$_3$ layers on the ridges and trenches are both given by $h_d = 70$ nm. Graphene is coated on top of the grating structure. The graphene layer adheres to YbF$_3$ on the ridges and suspends in air on the trenches of the grating. Detailed fabrication process of the hybrid structure is provided in Section 3. Figure 1c shows

the Raman spectrum of the transferred graphene on top of the grating. The graphene used in this work is grown by chemical vapor deposition (CVD) method.[32,33] The G and 2D peaks of the Raman shift are located at 1582 cm$^{-1}$ and 2668 cm$^{-1}$, respectively. The intensity of 2D peak is 3.84 times stronger than that of the G ($I_{2D}/I_G$) peak, indicating that the graphene is monolayer. It should be mentioned that the D peak (1350 cm$^{-1}$) is absent in the Raman spectrum, implying that there are very few defects in the graphene. We also scanned the uniformity of graphene layer by Raman microscopy. The monolayer graphene appears fairly homogeneous in a large area, as shown in Figure S5, Supporting Information. According to the ratio of 2D and G peaks intensities, the electron concentration can be inferred as $n_e = 5 \times 10^{12}$ cm$^{-2}$.[34,35] The chemical potential of graphene is then given by $\mu_c = \hbar v_F (\pi n_e)^{1/2} = 0.26$ eV, where $v_F = 10^6$ ms$^{-1}$ is the Fermi velocity. The electrical characterization of graphene was completed by a graphene device on top of a silicon substrate covered with 90 nm of SiO$_2$ (see Supporting Information). As shown in Figure 1d, the mobility of electrons in graphene is measured as a function of gate voltage applied between graphene and the heavily doped Si substrate. The Al$_2$O$_3$ film is used to eliminate scattering effect from air, which has led to an n-doping to the measurement graphene device. The observation of field effect mobility of graphene is $\mu \approx 3000$ cm$^2$ V$^{-1}$ s$^{-1}$. The momentum relaxation time is calculated by $\tau = \mu_c \mu/(e v_F^2) = 0.073$ ps.[34]

**ADVANCED
SCIENCE NEWS**

www.advancedsciencenews.com

LASER
&PHOTONICS
REVIEWS

www.lpr-journal.org

**Figure 2.** a) Experimental setup of PiFM. The incident laser generated by a QCL is focused on the sample/tip regime by a parabolic mirror (NA = 0.75). The QCL is operated in pulsed mode, with the pulse frequency equal to $f_m$. b) AFM topography image of the measured sample. c) PiFM image at $k = 1516$ cm$^{-1}$.

In the mid-infrared range, the wave vector of GPs on the graphene support by a dielectric can be expressed as[12]

$$k_{GP} \approx i(1 + \varepsilon_d)k_0/(\sigma_g \eta_0) \qquad (1)$$

where $k_0$ is the incident wavenumber in air, $\eta_0$ stands for the impedance, and the surface conductivity of graphene is given by $\sigma_g = ie^2\mu_c/[\pi\hbar^2(\omega + i\tau^{-1})]$ with $\mu_c$ being the chemical potential of graphene and $\tau$ the momentum relaxation time.[36] Therefore the wavelength of GPs is arrived at $\lambda_{GP} = 2\pi/\text{Re}(k_{GP})$. An obliquely incident laser beam of transverse magnetic (TM)-polarization is focused to the sample area near the metallic tip by a parabolic mirror (NA = 0.75). The tip could act as an optical antenna and scatters incident light to compensate the required wave vector for exciting the GPs, as illustrated in Figure 1a. Consequently, as the tip moves on the surface of the hybrid structure, the GPs should be launched on the ridge and trench areas of the grating. As the doping levels of graphene in the ridge and trench are different and GPs are sensitive to the geometric structure, the two regions have their respective response wavelengths.[35] The GPs are also reflected and scattered by internal boundaries, defects, and other structural discontinuities.
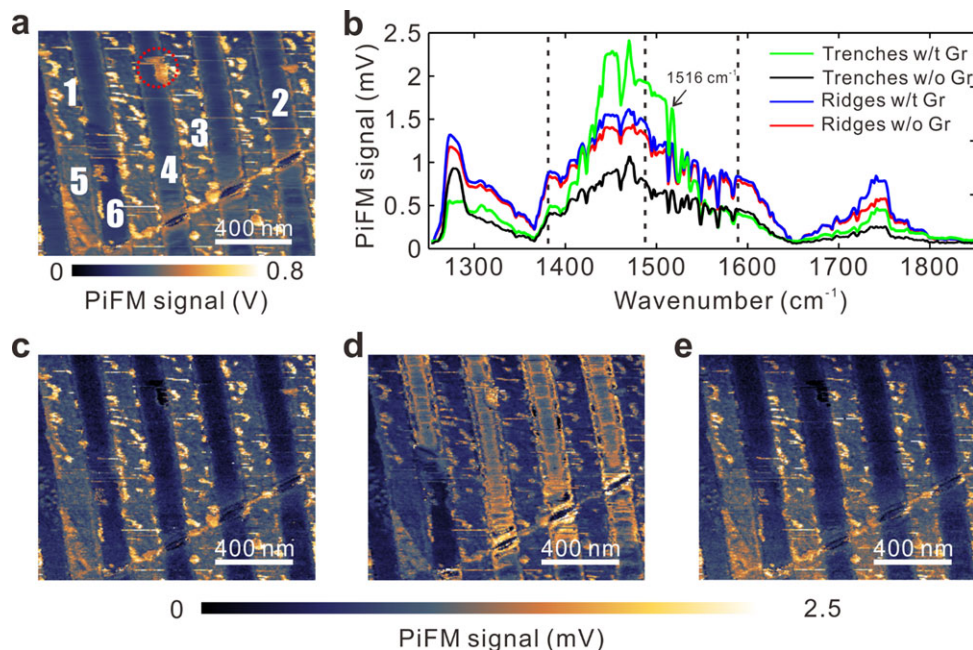
In order to characterize the GPs on graphene, we employ a recently developed technique PiFM to detect the optical force gradient between the GPs and a metallic tip. The schematic diagram of the PiFM is illustrated in **Figure 2**a. The incident light is generated by a quantum cascade laser (QCL) with the wavenumber adjustable in a wide range from 850 to 1850 cm$^{-1}$. For the purpose of exciting GPs and driving dipoles at the metallic tip, the incident laser beam should be TM polarized so that the dominating component of the electric field is normal to graphene. As the resonance condition is satisfied, the electric field of GPs will strongly interact with the induced dipole in the metallic tip which is connected with a cantilever. The cantilever is

operated in a dynamic (AC) mode with an oscillation frequency $f_1$. To amplify the optical force and enhance the electrical field of the excited GPs, the incident light is modulated at the sideband frequency $f_m$ by an acousto-optic modulator (AOM). Under the modulation, the cantilever could be excited at the fundamental resonance frequency $f_0 = f_1 \pm f_m$ due to the mixing of the modulated dipole–dipole signals (one modulation is due to the laser amplitude modulation and the other is the modulation due to the changing tip-sample distance of the AC mode AFM). By detecting the oscillation amplitude of the cantilever at the two frequency channels ($f_1$ and $f_0$), the topography and optical force can be obtained simultaneously, respectively.[31,37]

Figure 2b shows the topography of the sample. The alternately bright and gray fringes clearly show the ridge and trench areas of the grating. The ridge areas are about 21 nm higher than the trench areas. The depth is much larger than the negligible polymethyl methacrylate (PMMA) residue on the top of graphene.[38,39] The relatively darker ridge areas A and C are about 85 nm lower than the nearby trench, indicating that the graphene layer is broken in these regions. The bright area B indicates that the nature of graphene layer may be different compared to the other ridge parts of the sample (see Supporting Information). There are also several scratches along a line, which make an angle $\alpha$ with the perpendicular direction of the grating. The scratches could act as scatters and allow us to evaluate the propagation loss of GPs. The PiFM signal for the same sample region of Figure 2b obtained at frequency $f_0$ is shown in Figure 2c. The corresponding wavenumber of incident light is given by $k = 1516$ cm$^{-1}$. The detected PiFM image is a superposition of the photo-induced dipole force gradient of the intrinsic sample that is expected to be largely dependent of the electric field intensity of GPs in the normal direction. It can be seen from Figure 2c that the GPs exhibit an edge mode from every border of the trenches and ridges which is due to the reflection at the edge.[25] The fringes demonstrate the interference of the reflected GPs. This edge mode corresponds to a sharp resonance peak in the PiFM spectrum as shown in **Figure 3**b, which indicates that the GP excitation efficiency is high at frequencies near to 1516 cm$^{-1}$. As reported in previous works, the wavenumbers for efficiently exciting GPs on SiC and SiO$_2$ substrates should be around 1030 cm$^{-1}$ and 892 cm$^{-1}$, respectively.[23,24] The chemical potential of graphene is related largely to the substrate. The YbF$_3$ substrate and the grating structure beneath graphene results in a different wavenumber range for exciting GPs with high efficiency. We also perform experiments in the range 850–1250 cm$^{-1}$, where the PiFM signal is very weak, suggesting the low excitation efficiency of GPs (see Supporting Information). There are very poor signals detected in the area corresponding to areas A and C in Figure 2b. It is consistent with the topography that suggests broken graphene layer in these areas. We also note that the GPs are enhanced at the scratches since they experience strong local scattering.

Figure 3a displays the hyper-spectral infrared (hyPIR) image of the sample, which is obtained by summing the PiFM signals at each point of the measured area. From the image, one can evaluate the overall optical force response of GPs in the considered wavenumber range. Generally, in the hyPIR image, the PiFM signal has a larger amplitude on the ridges (areas 1, 3, and 5) than the trenches. PiFM signals throughout the ridges are affected by a series of dielectric roughness, which generated

# ADVANCED
## SCIENCE NEWS
www.advancedsciencenews.com

LASER
& PHOTONICS
REVIEWS

www.lpr-journal.org

**Figure 3.** a) hyPIR image generated by PiFM. b) PiFM spectra for the wavenumber range from 1250 cm$^{-1}$ to 1850 cm$^{-1}$. The green spectrum is generated by averaging the PiFM signals in the trench regions as marked by 2 and 4. The black spectrum is obtained by averaging the PiFM signals in the missing graphene region as marked by 6. The blue spectrum shows the average PiFM signal of the ridge region covered by graphene as marked by 1 and 3. The red spectrum shows the PiFM signal of the ridge region without graphene as marked by 5. c–e) PiFM images for different wavenumbers: c) $k = 1380$ cm$^{-1}$, d) $k = 1496$ cm$^{-1}$, and e) $k = 1591$ cm$^{-1}$.
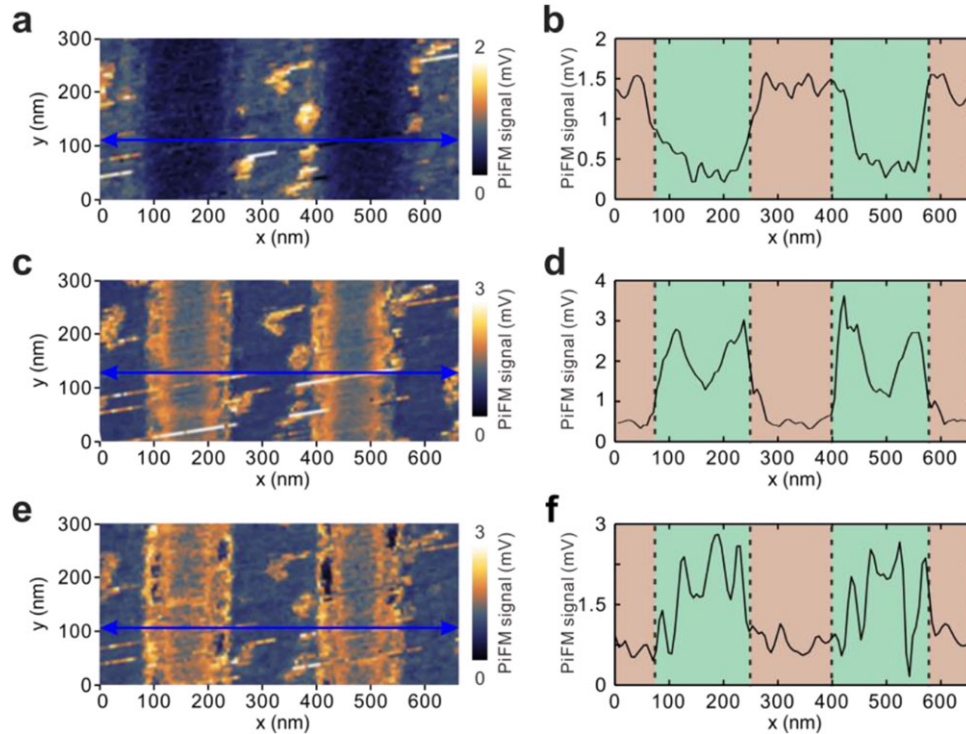
from the deposition process. The contaminant that is noted by a dashed circle has a strong response at a wavenumber of 1746 cm$^{-1}$ as shown in Figure S4, Supporting Information.

The average PiFM spectra for the ridge, trench, and graphene-broken areas are shown together in Figure 3b. The coincident dips in the PiFM spectra are due to the water absorption of the mid-IR laser since the experiment is conducted in air. The video file (see Supporting Information) shows the GP progression as the wavenumber is swept through the entire region. Comparing the spectra from different areas of the sample, we notice that the PiFM signal of the dielectric is higher than the signal of the graphene at the wavenumber range from 1250 cm$^{-1}$ to 1430 cm$^{-1}$ and the range from 1520 cm$^{-1}$ to 1850 cm$^{-1}$. The PiFM signal of areas 1, 3, and 5 is stronger than that of the areas 2 and 4 in these wavenumbers. The reason is due to the interaction between the induced dipoles of dielectric layer and the metallic tip, in addition to that of GPs and the latter. We note that the signal level at the area 5 is pretty much the same as the other ridges where graphene layer is intact. Additionally, the video file also confirms that area 5 behaves similar to the other ridges throughout the entire spectral range, indicating that the height difference in area 5 is most likely due to thicker dielectric layer and not missing graphene layer. All spectra have a strong peak with a center wavenumber at 1276 cm$^{-1}$, except for the spectrum of trenches with graphene of areas 2 and 4 in Figure 3a. It can be explained that the dielectric layer is polarized by the excitation light. For the graphene missing trench (area 6), PiFM spectrum always shows a lower intensity than other tested areas in the dielectric material surface. The PiFM signal on the trenches with graphene (areas 2 and 4) is much stronger than that on the ridges at the wavenum-

bers from 1430 cm$^{-1}$ to 1520 cm$^{-1}$. This is due to the distinct resonance of GPs on the trenches and ridges of the grating.

Figure 3c shows the PiFM signal of the sample at $k = 1380$ cm$^{-1}$, where the GPs are mostly concentrated on the ridges. As the wavenumber becomes $k = 1496$ cm$^{-1}$, the resonance of GPs occurs on the trenches and the optical force is enhanced, as shown in Figure 3d. Note that there are still noisy spots on the ridges areas, which indicate the influence of the dielectric layer. Although the areas A and C are located on the trench, there are no signals here due to the damaged graphene. When the wavenumber keeps increasing to $k = 1591$ cm$^{-1}$, the resonance occurs on the ridges again and the PiFM signal becomes stronger, as shown in Figure 3e.

In order to characterize the GPs more precisely, we focus on a fixed area to investigate the PiFM signals on the ridges and trenches. **Figure 4**a shows the PiFM signal at $k = 1380$ cm$^{-1}$ within an area of two grating periods. The field is mainly concentrated on the ridges at the given wavenumber. The lateral profile of the PiFM signal is plotted in Figure 4b. It clearly shows that the PiFM signals are almost uniform on the ridges, excluding the noisy bright spots. As the graphene layer adheres to the dielectric of YbF$_3$, the loss of GPs is larger than that on trenches and the signals should be associated more closely with the dipoles in the dielectric. It is also the reason for the appearance of bright noise on the ridges. Therefore, we concentrate on the GPs excited on the trenches of the grating. Figure 4c shows the PiFM signal at $k = 1446$ cm$^{-1}$. One sees clearly the interference fringes of the GPs. The minimum intensity lies in the center of the trenches where the GPs experience destructive interference. The lateral profile corresponding to the blue arrow is shown in Figure 4d.

**ADVANCED
SCIENCE NEWS**

www.advancedsciencenews.com

LASER
&PHOTONICS
REVIEWS

www.lpr-journal.org

**Figure 4.** a) PiFM signals at $k = 1380$ cm$^{-1}$. The YbF$_3$ material doped graphene which is located at the ridge area is polarized. b) Lateral profile along the blue arrow in Figure 4a. PiFM signals at c) $k = 1446$ cm$^{-1}$ and e) 1496 cm$^{-1}$, respectively, show the low-frequency GP interference mode and the high-frequency GP interference mode. d) Lateral profile along the blue arrow in Figure 4c at $k = 1446$ cm$^{-1}$. f) Lateral profile along the blue arrow in Figure 4e at $k = 1496$ cm$^{-1}$. All images of (a), (c), and (e) were taken at the same location on the surface of the sample. In (b), (d), and (f), the green and orange regions represent the trench and ridge areas of the grating, respectively.

Using $\tau = 0.073$ ps and $\mu_c = 0.26$ eV, we get the wavelength of GPs $\lambda_{GP} \approx 142$ nm at wavenumber $k = 1446$ cm$^{-1}$ from Equation (1), which is roughly twice the width of the fringes in Figure 4c. Continuous tunable light frequency can excite the high order GP interference mode in a high frequency. Figure 4e shows the PiFM signal at $k = 1496$ cm$^{-1}$. There are also several bright fringes located away from the trench edges where the GPs are enhanced due to constructive interference. The lateral profile as marked by the blue arrow is shown in Figure 4f. The average width of the fringe itself and the width between the fringes are 43 and 67 nm, respectively. Thus the wavelength of GPs is 110 nm, which agrees well with the numerical result of 112 nm from Equation (1) at 1496 cm$^{-1}$.
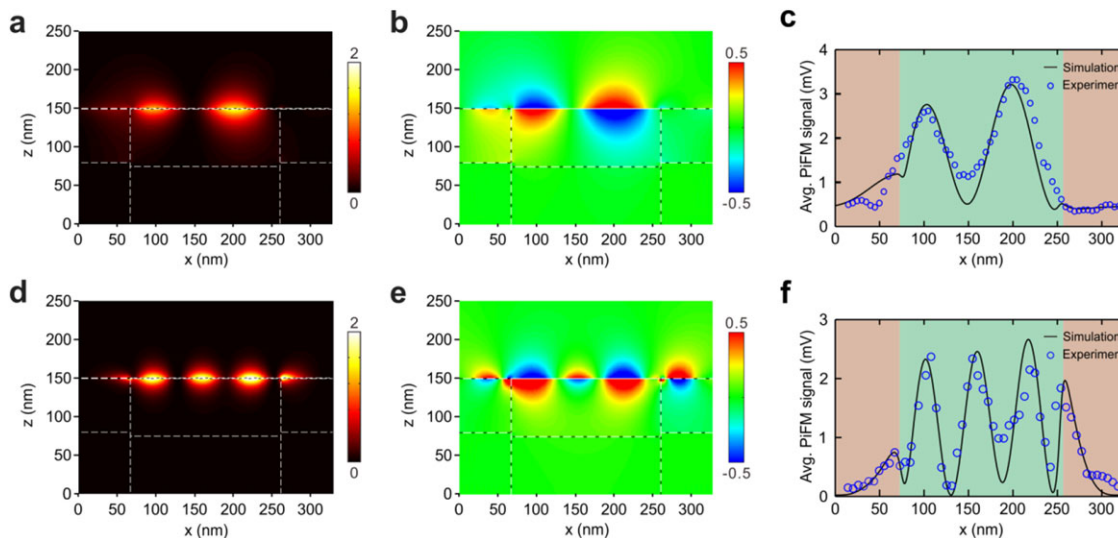
We also perform numerical calculation to evaluate the field distribution of GPs in the trenches by using a rigorous coupled wave analysis (RCWA) method, as shown in **Figure 5**. In the calculation, the graphene layer with $\tau = 0.073$ ps and $\mu_c = 0.26$ eV is the none-doped graphene, and the YbF$_3$ layer with a refractive index of $n_d = 1.5 - 0.5i$ is the highly doped medium. The incident angle of the TM polarized plane wave is set as 70° in accordance with the experiment. Figure 5a,d shows the intensity distribution ($|E_z|^2$) of GPs in the $x$–$z$ slice with wavenumbers at 1446 cm$^{-1}$ and 1496 cm$^{-1}$, respectively. Electric field ($E_z$) distribution of the GPs for this two interference modes are shown in Figure 5b,d. We randomly select ten sets of PiFM data from Figure 4c,e to get the average PiFM signal as the GP amplitude distribution from two interference modes. The calculated lateral profiles together

with the experimental data in a single trench are plotted in Figure 5c,f. They coincide well with each other.

The loss of the GPs has also been studied by investigating the decay of GPs along the grating. The scratches as shown in Figure 1c will scatter the GPs along the $y$-direction, which will interfere with the excited GPs along the $x$-direction. The inset of **Figure 6**a shows a schematic of interference in two directions. The field intensity of the GPs along the grating should be approximately given by

$$I(y) = |E_z|^2$$
$$= A_t^2 + A_s^2 \exp(-2\gamma y) + 2 A_t A_s \exp(-\gamma y) \cos(k_{GP} y \cos\alpha)$$

$$(2)$$

where $A_t$ and $A_s$ represent the amplitudes of GPs by the trench edges and the scratches, respectively. The decay coefficient along the $y$-direction is denoted by $\gamma$. Figure 6a shows the PiFM signal distribution along the $y$-direction at $k = 1496$ cm$^{-1}$. The field experiences a slow decay with oscillations. By fitting $A_t$ and $A_s$ according to Equation (2), we can obtain the theoretically predicted curve that agrees qualitatively well with the experimental result. The propagation distance of the GPs is about $L_{GP} = 173.3$ nm. As the wavenumber increases to 1510 cm$^{-1}$, one sees that the propagation distance becomes smaller and the oscillation period decreases (Figure 6b). The result means that the loss of GPs

# ADVANCED
## SCIENCE NEWS

www.advancedsciencenews.com

LASER
& PHOTONICS
REVIEWS

www.lpr-journal.org

**Figure 5.** Numerical result for the intensity distribution ($|E_z|^2$) of interference GPs in the x–z plane at a) $k = 1446$ cm$^{-1}$ and d) 1496 cm$^{-1}$. Electric field ($E_z$) distribution of the GPs at b) $k = 1446$ cm$^{-1}$ and e) 1496 cm$^{-1}$. Profiles of the GPs for experimental (line of blue circles) and numerical results (black solid line) of $|E_z|^2$ distribution at c) $k = 1446$ cm$^{-1}$ and f) 1496 cm$^{-1}$.
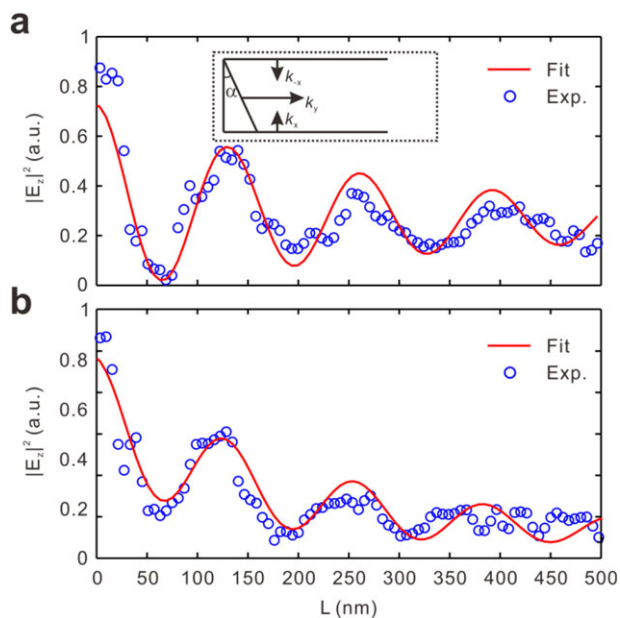


**Figure 6.** Experimental field intensity ($|E_z|^2$) and fitted curve along the y-direction. a) $k = 1496$ cm$^{-1}$, b) $k = 1510$ cm$^{-1}$. Here the experimental and fitted data are denoted by the red solid lines and blue circles, respectively.

increases at shorter wavelength. The measured propagation length is about $L_{GP} = 170.2$ nm.

## 3. Experimental Section

To fabricate sharp gold grating as resonator to excite the GPs, gold grating was prepared in a $150 \times 150$ $\mu$m$^2$ area at a double-sided polished silicon substrate using the standard electron beam lithography (EBL) and metal lift-off process. A 495PMMA-A-Resists (MicroChem) layer with a thickness of 240 nm was utilized as resist, which is fabricated by spin-coated and baked processes. After defining the grating patterns with high-resolution EBL (VISTEC EBPG 5000 PLUS), a nickel and gold film is deposited on the substrate by an electron beam evaporation (EBV) system (Ebeam-500S, Alpha-Plusco. Ltd). The thicknesses of the nickel and gold were 1 and 75 nm, respectively. Nickel layer was used to enhance adhesion between the silicon substrate and the gold grating. Gold grating was completed by lifting off the photoresist layer in acetone at 45 °C. The YbF$_3$ layer was deposited on the grating by thermal evaporation deposition with a thickness of 70 nm. The CVD grown monolayer graphene was transferred to the top of the YbF$_3$/grating structure with wet transfer techniques.[40] The copper foil is etched away in a 0.4 mol L$^{-1}$ ammonium persulfate (($NH_4$)$_2$S$_2$O$_8$) for 5 h. PMMA layer was removed by an acetone bath at 70 °C.

Monolayer graphene samples were grown on a 25 mm thick copper foil catalyst surface within a 4″ CVD reactor. The copper foil was processed in ($NH_4$)$_2$S$_2$O$_8$ for a few minutes first, the deionized (DI) water clean process was utilized to wash away the residual acid. Then the copper foil was annealed at 1035 °C for 60 min with argon in order to reduce the native copper oxide and increase the grain size. The graphene was grown at 1035 °C for 6 h using a mixture of methane and hydrogen (1:60) with argon as the gas carrier. After the growth stage, the CVD system was cooled down to room temperature under a hydrogen and argon atmosphere.

## 4. Conclusion

In conclusion, by using a newly developed PiFM technique, we have characterized precisely the GPs on graphene covering a

metallic grating. The PiFM measures the optical force between the GP field and the dipole in a metallic tip. As the force is proportional to the field intensity of GPs, it can provide high resolution measurement of field distribution without the influence of scattered field. By scanning the wavenumber of incident laser beam, the PiFM spectrum over a wide range can be obtained at each point on the sample, from which we find that the GPs are mainly concentrated on the trenches of the grating in the range from 1430 cm$^{-1}$ to 1510 cm$^{-1}$. It is found that the GPs experience interference in the trenches and the wavelength of the GPs can be obtained by measuring the interference pattern. By detecting the scattered field along the grating, the propagation distance of GPs can also be measured. The study indicates that PiFM technique has a great potential in precisely characterizing GPs at the deep subwavelength scale. It will also facilitate the design of nanoscale optical devices based on graphene.

## Supporting Information

Supporting Information is available from the Wiley Online Library or from the author.

## Acknowledgements

## Conflict of Interest

The authors declare no conflict of interest.

## Keywords

[1] J. A. Schuller, E. S. Barnard, W. Cai, Y. C. Jun, J. S. White, M. L. Brongersma, *Nat. Mater.* **2010**, *9*, 193.
[2] Q. Zhang, G. Li, X. Liu, F. Qian, Y. Li, T. C. Sum, C. M. Lieber, Q. Xiong, *Nat. Commun.* **2014**, *5*, 4953.
[3] M. Ozaki, J. Kato, S. Kawata *Science* **2011**, *332*, 218.
[4] B. Wang, A. B. Chew, J. H. Teng, G. Y. Si, A. J. Danner, *Appl. Phys. Lett.* **2011**, *99*, 151106.
[5] L. Li, T. Li, S. Wang, S. Zhu, X. Zhang, *Nano Lett.* **2011**, *11*, 4357.
[6] Q. Bao, K. P. Loh, *ACS Nano* **2012**, *6*, 3677.
[7] Y. J. Bao, S. Zu, Y. F. Zhang, Z. Y. Fang, *ACS Photonics* **2015**, *2*, 1135.
[8] Z. Fang, Y. Wang, Z. Liu, A. Schlather, P. M. Ajayan, F. H. Koppens, P. Nordlander, N. J. Halas, *ACS Nano* **2012**, *6*, 10222.
[9] H. Hu, X. Yang, F. Zhai, D. Hu, R. Liu, K. Liu, Z. Sun, Q. Dai, *Nat. Commun.* **2016**, *7*, 12334.
[10] F. Wang, C. Z. Qin, B. Wang, H. Long, K. Wang, P. X. Lu, *IEEE J. Sel. Top. Quant.* **2017**, *23*, 125.
[11] A. Vakil, N. Engheta, *Science* **2011**, *332*, 1291.
[12] M. Jablan, H. Buljan, M. Soljacic, *Phys. Rev. B* **2009**, *80*, 245435.
[13] Q. L. Bao, H. Zhang, Y. Wang, Z. H. Ni, Y. L. Yan, Z. X. Shen, K. P. Loh, D. Y. Tang, *Adv. Funct. Mater.* **2009**, *19*, 3077.
[14] Q. L. Bao, H. Zhang, B. Wang, Z. H. Ni, C. H. Y. X. Lim, Y. Wang, D. Y. Tang, K. P. Loh, *Nat. Photonics* **2011**, *5*, 411.
[15] W. Gao, G. Shi, Z. Jin, J. Shu, Q. Zhang, R. Vajtai, P. M. Ajayan, J. Kono, Q. Xu, *Nano Lett.* **2013**, *13*, 3698.
[16] H. Huang, S. L. Ke, B. Wang, H. Long, K. Wang, P. X. Lu, *J. Lightwave Technol.* **2017**, *35*, 320.
[17] Q. Liu, B. Wang, S. Ke, H. Long, K. Wang, P. Lu, *Opt. Express* **2017**, *25*, 7203.
[18] X. L. Zhu, W. Yan, P. U. Jepsen, O. Hansen, N. A. Mortensen, S. S. Xiao, *Appl. Phys. Lett.* **2013**, *102*, 131101.
[19] M. Farhat, S. Guenneau, H. Bagci *Phys. Rev. Lett.* **2013**, *111*, 237404.
[20] Z. Fang, Y. Wang, A. E. Schlather, Z. Liu, P. M. Ajayan, F. J. de Abajo, P. Nordlander, X. Zhu, N. J. Halas, *Nano Lett.* **2014**, *14*, 299.
[21] S. Ke, B. Wang, H. Huang, H. Long, K. Wang, P. Lu, *Opt. Express* **2015**, *23*, 8888.
[22] Z. Fei, A. S. Rodin, G. O. Andreev, W. Bao, A. S. McLeod, M. Wagner, L. M. Zhang, Z. Zhao, M. Thiemens, G. Dominguez, M. M. Fogler, A. H. C. Neto, C. N. Lau, F. Keilmann, D. N. Basov, *Nature* **2012**, *487*, 82.
[23] J. Chen, M. Badioli, P. Alonso-Gonzalez, S. Thongrattanasiri, F. Huth, J. Osmond, M. Spasenovic, A. Centeno, A. Pesquera, P. Godignon, A. Z. Elorza, N. Camara, F. J. Garcia de Abajo, R. Hillenbrand, F. H. Koppens, *Nature* **2012**, *487*, 77.
[24] P. Alonso-Gonzalez, A. Y. Nikitin, F. Golmar, A. Centeno, A. Pesquera, S. Velez, J. Chen, G. Navickaite, F. Koppens, A. Zurutuza, F. Casanova, L. E. Hueso, R. Hillenbrand, *Science* **2014**, *344*, 1369.
[25] J. A. Gerber, S. Berweger, B. T. O'Callahan, M. B. Raschke, *Phys. Rev. Lett.* **2014**, *113*, 055502.
[26] F. Huang, V. A. Tamma, Z. Mardy, J. Burdett, H. K. Wickramasinghe, *Sci. Rep.* **2015**, *5*, 10610.
[27] J. Jahng, J. Brocious, D. A. Fishman, F. Huang, X. W. Li, V. A. Tamma, H. K. Wickramasinghe, E. O. Potma, *Phys. Rev. B* **2014**, *90*, 155417.
[28] D. Nowak, W. Morrison, H. K. Wickramasinghe, J. Jahng, E. Potma, L. Wan, R. Ruiz, T. R. Albrecht, K. Schmidt, J. Frommer, D. P. Sanders, S. Park, *Sci. Adv.* **2016**, *2*, e1501571.
[29] T. U. Tumkur, X. Yang, B. Cerjan, N. J. Halas, P. Nordlander, I. Thomann, *Nano Lett.* **2016**, *16*, 7942.
[30] J. Kohoutek, D. Dey, A. Bonakdar, R. Gelfand, A. Sklar, O. G. Memis, H. Mohseni *Nano Lett.* **2011**, *11*, 3378.
[31] J. Jahng, B. Kim, E. S. Lee, E. O. Potma, *Phys. Rev. B* **2016**, *94*, 195407.
[32] X. Xu, Z. Zhang, J. Dong, D. Yi, J. Niu, M. Wu, L. Lin, R. Yin, M. Li, J. Zhou, S. Wang, J. Sun, X. Duan, P. Gao, Y. Jiang, X. Wu, H. Peng, R. S. Ruoff, Z. Liu, D. Yu, E. Wang, F. Ding, K. Liu, *Sci. Bull.* **2017**, *62*, 1074.
[33] X. Xu, Z. Zhang, L. Qiu, J. Zhuang, L. Zhang, H. Wang, C. Liao, H. Song, R. Qiao, P. Gao, Z. Hu, L. Liao, Z. Liao, D. Yu, E. Wang, F. Ding, H. Peng, K. Liu, *Nat. Nanotechnol.* **2016**, *11*, 930.
[34] A. Das, B. Chakraborty, S. Piscanec, S. Pisana, A. K. Sood, A. C. Ferrari, *Phys. Rev. B* **2009**, *79*, 155417.
[35] A. Das, S. Pisana, B. Chakraborty, S. Piscanec, S. K. Saha, U. V. Waghmare, K. S. Novoselov, H. R. Krishnamurthy, A. K. Geim, A. C. Ferrari, A. K. Sood, *Nat. Nanotechnol.* **2008**, *3*, 210.
[36] B. Wang, X. Zhang, F. J. Garcia-Vidal, X. Yuan, J. Teng, *Phys. Rev. Lett.* **2012**, *109*, 073901.

ADVANCED
SCIENCE NEWS

www.advancedsciencenews.com

LASER
& PHOTONICS
REVIEWS

www.lpr-journal.org

[37] J. Jahng, F. T. Ladani, R. M. Khan, X. Li, E. S. Lee, E. O. Potma, *Opt. Lett.* **2015**, *40*, 5058.

[38] Y. C. Lin, C. C. Lu, C. H. Yeh, C. Jin, K. Suenaga, P. W. Chiu, *Nano Lett.* **2012**, *12*, 414.

[39] Y. C. Lin, C. Jin, J. C. Lee, S. F. Jen, K. Suenaga, P. W. Chiu, *ACS Nano* **2011**, *5*, 2362.

[40] M. T. Ghoneim, C. E. Smith, M. M. Hussain, *Appl. Phys. Lett.* **2013**, *102*, 183115.

1800040 (8 of 8)